Journal of the Optical Society of America A
OPTICS, IMAGE SCIENCE, AND VISION

Strehl ratio: a tool for optimizing optical nulls and singularities

FRANÇOIS HÉNAULT

Institut de Planétologie et d'Astrophysique de Grenoble, Université Joseph Fourier, Centre National de la Recherche Scientifique, BP 53, 38041 Grenoble, France (francois.henault@obs.ujf-grenoble.fr)

Received 20 February 2015; revised 5 May 2015; accepted 18 May 2015; posted 18 May 2015 (Doc. ID 234926); published 16 June 2015

In this paper a set of radial and azimuthal phase functions are reviewed that have a null Strehl ratio, which is equivalent to generating a central extinction in the image plane of an optical system. The study is conducted in the framework of Fraunhofer scalar diffraction, and is oriented toward practical cases where optical nulls or singularities are produced by deformable mirrors or phase plates. The identified solutions reveal unexpected links with the zeros of type-J Bessel functions of integer order. They include linear azimuthal phase ramps giving birth to an optical vortex, azimuthally modulated phase functions, and circular phase gratings (CPGs). It is found in particular that the CPG radiometric efficiency could be significantly improved by the null Strehl ratio condition. Simple design rules for rescaling and combining the different phase functions are also defined. Finally, the described analytical solutions could also serve as starting points for an automated searching software tool.

OCIS codes: (050.1950) Diffraction gratings; (050.4865) Optical vortices; (070.0070) Fourier optics and signal processing; (350.1260) Astronomical optics; (350.4855) Optical tweezers or optical manipulation.

http://dx.doi.org/10.1364/JOSAA.32.001276

1. INTRODUCTION

During the past two decades, there has been a growing interest in optical systems enabling the creation of zero-irradiance nulls or "dark holes" at the center of their far-field intensity distributions. One may, for example, cite two types of applications sustaining quite different purposes:

– On the one hand, laser beams are sometimes carrying an orbital angular momentum (OAM) resulting in axial nulls, also named optical vortices or singularities and propagating over an infinite distance range. The produced intensity distributions exhibit unique properties exploitable in the fields of particle manipulation [1], nanotechnology, fundamental experiments in nonlinear and quantum optics [2], or superresolution [3]. Ways of generating such optical singularities are more or less simple, including deformable mirrors [4,5], discontinuous phase plates [6], synthetic holograms [7], spatial light modulators [8], and cylindrical lenses [9], or polarizing components integrated into interferometric setups [10,11]. They were the subjects of numerous other theoretical and experimental studies such as those summarized in the review paper [12] and its extensive list of bibliographic references.

– On the other hand, the recent discoveries of hundreds, and very soon thousands, of extrasolar planets and planetary systems strongly motivates developing new-generation space-based instrumentation, such as coronagraphs [13,14], enabling the spectral characterization of their atmospheres and the recognition of biologic life markers. Furthermore, a new class of coronagraphic instruments was proposed a few years ago [15–17], making use of optical vortices located at the telescope focal plane. Although the present study is limited to phase manipulation in the pupil plane, we believe that it can easily be transposed into the telescope image plane without loss of generality.

In this paper a simple and common approach is presented for better understanding and optimizing the intensity distributions generated by an optical system for both types of applications, also having in mind practicable technical solutions based on a deformable mirror or phase plates. Incidentally, this study will be restricted to optical nulls formed in the vicinity of the image plane of the system, not addressing the question of their stability in an optical cavity or an optical waveguide, where they must be solutions of the Helmholtz differential equation.

The present paper is organized as follows: Section 2 presents the necessary conditions for obtaining a central null in the image plane, derived from a classical expression of the Strehl ratio. Trivial solutions of these equations are described in Section 3, including pure azimuthal and axis-symmetric phase distributions onto a circular pupil. Section 4 deals with the specific case of circular gratings with equally spaced lines, while the effects of more complex aperture shape and arrangement are discussed in Section 5. Finally, a short conclusion is provided in Section 6.

2. GENERAL RELATIONS AND PROPERTIES

The theoretical framework of the present study is restricted to first-order Gaussian optics and Fraunhofer scalar diffraction. The following topics are not covered here: vectorial models describing wave polarization effects, high numerical aperture optical systems, and extension to Fresnel diffraction domain—all subjects that may be the scope of future work. The study is also limited to the monochromatic case, with the exception of Section 4 dealing with circular gratings.

The coordinate systems and scientific notations employed throughout this paper are indicated in Fig. 1. They essentially consist of two normal reference frames $(OXYZ)$ and $(O'X'Y'Z')$, where Z is the optical axis of the system and the (OX, OY) and $(O'X', O'Y')$ planes are attached to its output pupil and image plane, respectively. It is assumed that the output pupil is limited by a circular aperture of radius R, enclosing points P denoted either by their Cartesian coordinates (x, y) or by their polar coordinates (r, θ). In the image plane $O'X'Y'$ located at a distance F from the exit pupil, points M' are denoted by their Cartesian coordinates (x', y'). Practically, we are mainly concerned with the luminous intensity observed at its center O', whose coordinates are by definition (0,0).

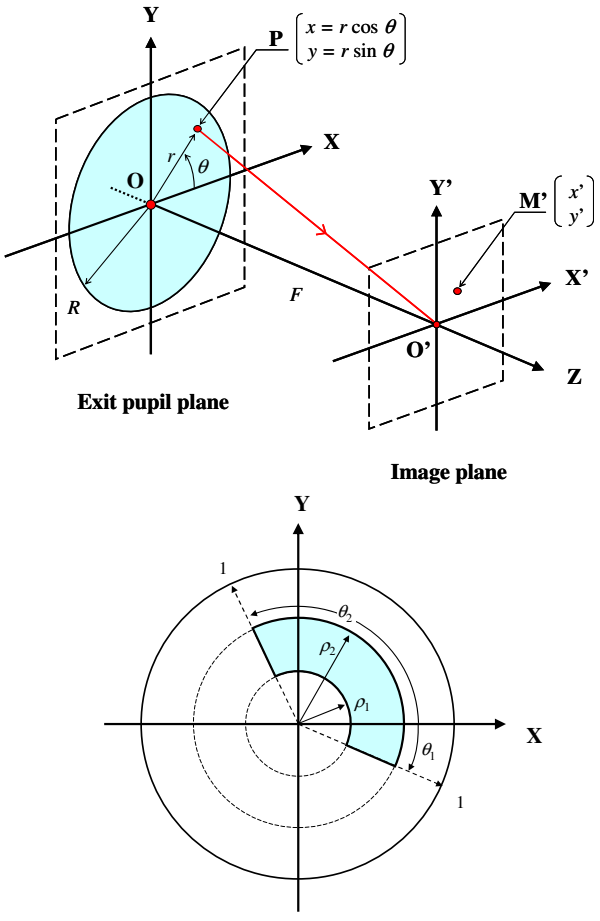

Fig. 1. Coordinate systems and scientific notations. (Top) Main employed coordinates. (Bottom) Case of segmented subpupils as discussed in Section 5.

The starting point of this study is the Strehl ratio (SR), a widely used metric evaluating the image quality of an optical system. Assuming weak aberrations and/or shape errors $\Delta(x, y)$ in the exit pupil of the system, SR is classically defined as the ratio

$$\mathrm{SR} = \mathrm{Max}[\mathrm{PSF}_\Delta(x', y')]/\mathrm{PSF}_0(0, 0), \tag{1}$$

where $\mathrm{PSF}_\Delta(x', y')$ is the point spread function of the optical system in the presence of the wavefront errors $\Delta(x, y)$, $\mathrm{Max}[\mathrm{PSF}_\Delta(x', y')]$ is the peak value of the PSF in the image plane, usually located at O', and $\mathrm{PSF}_0(x', y')$ is the ideal PSF of the optical system free of aberrations, assuming $\Delta(x, y) = 0$ over the full exit pupil. Here, it is equal to the Airy intensity distribution $|2J_1(r')/r'|^2$, where J_1 is the type-J Bessel function at the first order, $r' = 2\pi R\sqrt{x'^2 + y'^2}/\lambda$, and λ is the wavelength of the electromagnetic field (assumed to be monochromatic).

As in [18,19], we assume that $\mathrm{Max}[\mathrm{PSF}_\Delta(x', y')] = \mathrm{PSF}_\Delta(0, 0)$; therefore, from an elementary property of Fourier transformation,

$$\mathrm{SR} = \left| \iint_{\substack{\text{Pupil}\\ \text{aperture}}} t(x,y)\exp[2i\pi\Delta(x,y)/\lambda]\mathrm{d}x\mathrm{d}y \Big/ \Big/ \iint_{\substack{\text{Pupil}\\ \text{aperture}}} t(x,y)\mathrm{d}x\mathrm{d}y \right|^2, \tag{2}$$

where $t(x, y)$ is a real function defined over the whole pupil area, usable for introducing pupil masks or continuous amplitude apodization, and $i = \sqrt{-1}$.

For what follows, successive assumptions and changes of notations are made:

(1) Replace the wavefront error $\Delta(x, y)$ with its associated phase function $\varphi(x, y) = 2\pi\Delta(x, y)/\lambda$.

(2) Move from Cartesian coordinates (x, y) to polar coordinates (r, θ), and replace the differential elements $\mathrm{d}x\mathrm{d}y$ with $r\mathrm{d}r\mathrm{d}\theta$.

(3) Replace r with a reduced radial coordinate $\rho = r/R$ along the pupil radius R, with $0 \le \rho \le 1$.

(4) Assume that the resulting phase distribution $\varphi(\rho, \theta)$ can be expressed as the product of two single-variable phase functions, writing: $\varphi(\rho, \theta) = \varphi_r(\rho) + \varphi_a(\theta)$.

(5) Assume as well that the transmission function can be expressed as $t(\rho, \theta) = t_r(\rho)t_a(\theta)$.

One may consider assumptions 4 and 5 as too restrictive (excluding, for example, coma or astigmatism-like functions) and artificially limiting the domain of eligible phase distributions for generating central nulls. It seems, however, that this domain remains vast enough for studying a variety of cases presented in the forthcoming Sections 3 and 4. In addition, the practical realization of axis-symmetric functions $\varphi_r(\rho)$ and $t_r(\rho)$ may prove much easier by means of current technology. Therefore, the SR in Eq. (2) can be rewritten as

$$SR = \left| \int_{\rho=0}^{1} t_r(\rho) \exp[i\varphi_r(\rho)]\rho \mathrm{d}\rho \Big/ \int_{\rho=0}^{1} t_r(\rho)\rho \mathrm{d}\rho \right|^2 \times \left| \int_{\theta=0}^{2\pi} t_a(\theta) \exp[i\varphi_a(\theta)]\mathrm{d}\theta \Big/ \int_{\theta=0}^{2\pi} t_a(\theta)\mathrm{d}\theta \right|^2 = |S_r S_a|^2, \tag{3}$$

where the integrals S_r and S_a can respectively be defined as the "radial" and "azimuthal" Strehl ratios in amplitude, being equal to

$$S_r = \int_0^1 t_r(\rho) \exp[i\varphi_r(\rho)]\rho \mathrm{d}\rho \Big/ \int_0^1 t_r(\rho)\rho \mathrm{d}\rho, \tag{4a}$$

$$S_a = \int_0^{2\pi} t_a(\theta) \exp[i\varphi_a(\theta)]\mathrm{d}\theta \Big/ \int_0^{2\pi} t_a(\theta)\mathrm{d}\theta. \tag{4b}$$

The case of a uniformly illuminated and unvignetted pupil is of particular interest, because it offers the best radiometric efficiency, and will serve as basis for this study. It follows that $t_r(\rho)$ and $t_a(\theta)$ are equal to unity over the full exit aperture, and Eqs. (3) and (4) are rewritten as

$$\mathrm{SR} = |S_r S_a|^2/\pi, \tag{5a}$$

$$S_r = \int_0^1 \exp[i\varphi_r(\rho)]\rho \mathrm{d}\rho, \tag{5b}$$

$$S_a = \int_0^{2\pi} \exp[i\varphi_a(\theta)]\mathrm{d}\theta. \tag{5c}$$

It can be concluded that searching for phase functions $\varphi_r(\rho)$ or $\varphi_a(\theta)$ satisfying to the conditions $S_r = 0$ or $S_a = 0$ allows achieving PSF intensity distributions exhibiting an axial null, or zero-irradiance at the center. Section 3 is entirely devoted to identifying trivial solutions to these equations. However, three interesting properties of these phase functions can already be derived from Eq. (5a):

- P1. Any axis-symmetric, or radial phase function $\varphi_r(\rho)$ will not destroy the central null generated by an azimuthal phase function $\varphi_a(\theta)$ satisfying to $S_a = 0$, when they are added together at the pupil plane.
- P2. Similarly, azimuthal phase functions $\varphi_a(\theta)$ will not affect the central null generated by a radial phase function $\varphi_r(\rho)$ fulfilling $S_r = 0$.
- P3. Because $|S_a|$ and $|S_r| \leq 1$, the null depth generated by any of two azimuthal or radial functions $\varphi_a(\theta)$ and $\varphi_r(\rho)$ can only be enhanced when they are added together at the pupil plane.

Alternatively, properties P1 and P2 may be reworded as follows:

- P11′. Any axis-symmetric phase function $\varphi_r(\rho)$ can be modified so as to generate an axial null, by adding an azimuthal phase function $\varphi_a(\theta)$ satisfying to $S_a = 0$.
- P22′. Similarly, any azimuthal phase function $\varphi_a(\theta)$ can be modified so as to generate an axial null, by adding a radial phase function $\varphi_r(\rho)$ fulfilling $S_r = 0$.

3. TRIVIAL SOLUTIONS

Subsections 3.A and 3.B examine and discuss trivial solutions to the zero-irradiance conditions $S_a = 0$ and $S_r = 0$ for azimuthal phase functions $\varphi_a(\theta)$ and axis-symmetric phase functions $\varphi_r(\rho)$, respectively.

A. Azimuthal Phase Functions

From Section 2, azimuthal phase functions $\varphi_a(\theta)$ generating on-axis null in the image plane of an optical system must fulfill the necessary condition:

$$S_a = \int_0^{2\pi} \exp[i\varphi_a(\theta)]\mathrm{d}\theta = 0. \tag{6}$$

Trivial solutions for the phase functions $\varphi_a(\theta)$ can be constructed from an integral representation of the type-J Bessel functions of integer order m [20]:

$$J_m(z) = \frac{1}{2k\pi i^m} \int_{\frac{l\pi}{2}}^{\frac{l\pi}{2}+2k\pi} \exp[i(z\cos t + mt)]\mathrm{d}t, \tag{7}$$

where k and l also are integers with $k > 1$ and $0 \leq l \leq 3$. Setting $t = k\theta + l\pi/2$ in the integral of Eq. (7) and rewriting S_a as $S_a(z)$ yields

$$S_a(z) = 2\pi i^m J_m(z) \exp[-iml\pi/2] = \exp[-iml\pi/2] \int_0^{2\pi} \exp[i\{z\cos(k\theta + l\pi/2) + mk\theta\}]\mathrm{d}\theta. \tag{8}$$

Then the condition $S_a(z) = 0$ shall be respected if

$$\varphi_a(\theta) = z_{m,n} \cos(k\theta + l\pi/2) + mk\theta, \tag{9}$$

where $z_{m,n}$ is the nth zero of the type-J Bessel function $J_m(z)$. For commodity of notation we can set $z_{m,0} = 0$ when $m \neq 0$, because the $J_m(z)$ functions—excepting $J_0(z)$—are equal to zero at the origin. Additionally, Eq. (8) reveals the presence of a "Gouy-like" phase-shift term equal to $-m(1 + l)\pi/2$, that will be ignored in the remainder of the text.

To summarize, Eq. (9) defines a family of phase functions $\varphi_a(\theta)$ generating axial nulls at the focus of any optical system, and being characterized with four integer numbers m, n, k, and l:

- m is the order of the phase function, giving rise to linear phase ramps in azimuth;
- n is related to the amplitude of the cosine modulation term of the phase function;
- k is proportional to the number of oscillations of the cosine phase term, and to the amplitude of the linear ramp; and
- l is a phase-shift index associated with the cosine modulation term.

Setting different criteria upon the previous indices allows defining two basic classes of nulling azimuthal phase functions, from which a quasi-infinite number of combinations can be inferred. By convention, it is assumed that $z_{0,0} = 0$, hence $\varphi_a(\theta) = 0$ and no central null is generated in that case.

1. Optical Vortex of Integer Order m

Let us consider the case when $m \neq 0$ and $n = 0$. Since $z_{m,0} = 0$, it is then found that $\varphi_a(\theta) = mk\theta$, which is indeed the linear phase ramp giving birth to an optical singularity of topological charge mk [12]. This type of intensity distribution is already well characterized and probably does not deserve additional graphic representations. This first solution, however, allows illustrating one of the three properties mentioned in Section 2, namely P1, stating that an additional axis-symmetric wavefront error (WFE) term should not affect the null generated on-axis by an azimuthal phase function. We choose an optical vortex of topological charge 4, and show in Fig. 2 the effects of a variable amount of defocus on the resulting PSF intensity distributions. Several elements are displayed:

– Panel A displays a gray-scale map of the PSF generated by the ideal phase ramp. The mathematical properties of this type of intensity distribution are very similar to those of laser beams' optical vortices [12] and were also discussed in [21] for the case of a uniformly illuminated pupil being considered here. The X' and Y' axes in this figure are scaled in terms of λ/D, as well as in all other PSF vignettes depicted in the present paper. Their side length is equal to $128\lambda/D$.

– Panels B and C show gray-scale maps of the PSF generated by the same phase ramp, defocused by $+2\lambda$ and $+4\lambda$, respectively. While the axial null is preserved as expected, one also distinguishes an apparent enlargement of the dark central region.

– Panel D simulates an interferogram of the same phase ramp defocused by $+4\lambda$. One notes its spiral-like aspect suggesting a possible definition of the spiral phase distributions as the association of a linear azimuthal phase ramp with any type of axis-symmetric function.

– Finally, Panels E and F depict intensity slices of the three PSFs (A, B, and C) along the X'-axis (marked by thin white lines in panels A, B, and C). In Fig. 2(E), the curves' maxima have been arbitrarily set to 1, while in Fig. 2(F) they are normalized in energy and plotted in logarithmic scale. The latter confirm that the darkened area slightly increases with defocus.

All the PSFs were computed numerically, using a fast Fourier transform algorithm with a pupil sampling of at least 512×512 and a zero-padding factor of 4 to avoid aliasing effects. These characteristics remain the same throughout the whole study. It has also been checked that higher pupil sampling is required when greater integer numbers m, n, and k are considered, typically superior to 10.

2. Azimuthal Cosine Modulation

In this case, we set the index $m = 0$; therefore, the azimuthal phase function is equal to $\varphi_a(\theta) = z_{0,n} \cos(k\theta + l\pi/2)$, where the linear phase term in θ vanishes, and only the zeros of the Bessel function $J_0(z)$ need to be considered. The general aspect of this type of phase distribution is illustrated in Fig. 3. Here

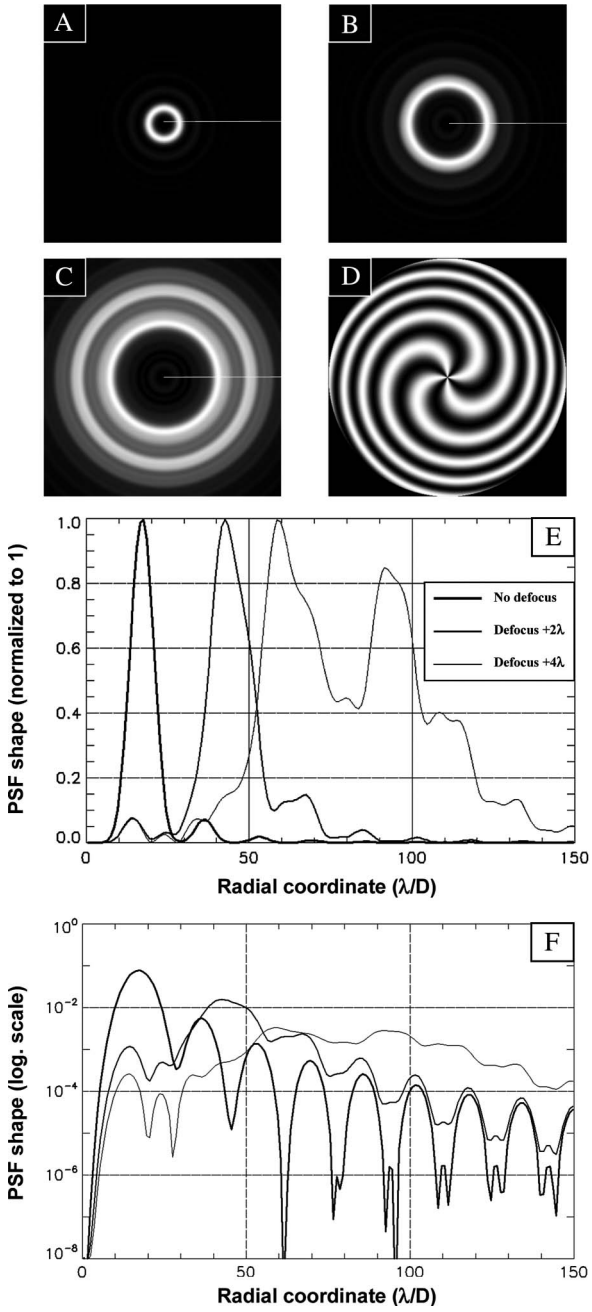

Fig. 2. Intensity distributions of a defocused optical vortex of topological charge 4. A, ideal PSF; B, defocused PSF by $+2\lambda$; C, defocused PSF by $+4\lambda$; D, interferogram associated with C; E, X'-slices of PSF A, B, and C along the thin white lines (linear scale); F, same curves as in E with logarithmic scale. The X' and Y' axes are scaled in terms of λ/D, and the side length of vignettes A, B, and C is $128\lambda/D$.

the WFE appear as classical Siemens star test patterns (used for optical component characterization). The figure also depicts the associated interferograms, to which were added two fringes of vertical tilt for the sake of illustration. When compared to the classical optical vortex discussed above, the azimuthal cosine modulation shows no 2π-phase jumps or discontinuity in the XY plane, except at the origin O where it could be eliminated by piercing a central hole (see Subsection 5.A dealing

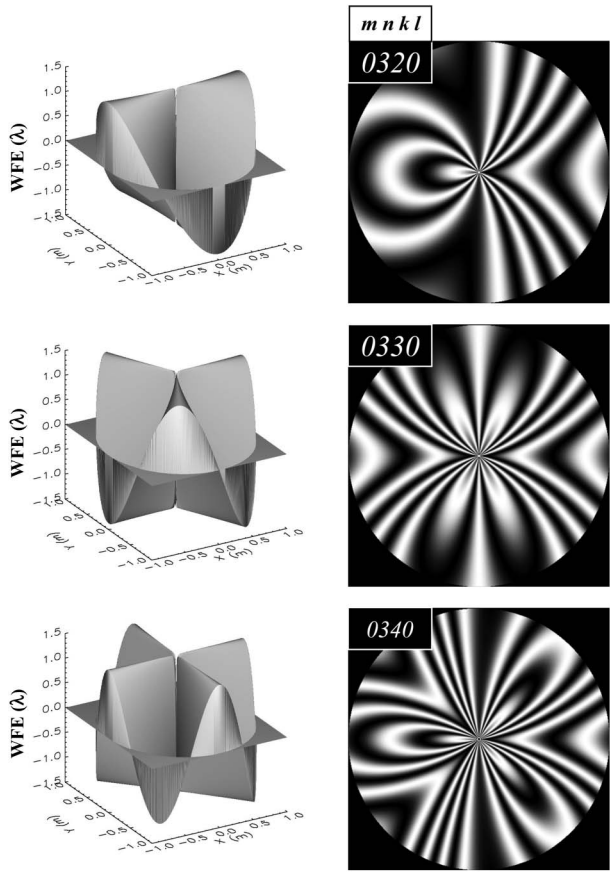

Fig. 3. Examples of periodic azimuthal phase functions (3D plots) and their interferograms. The four digits indicate the index values m, n, k, and l. Interferograms are simulated with two fringes of vertical tilt each.

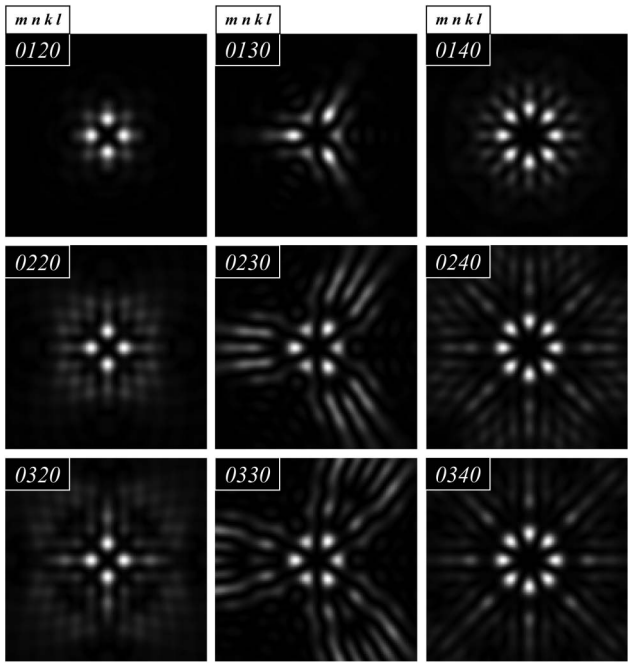

Fig. 4. Intensity distributions produced by periodic azimuthal phase functions. The four digits indicate the index values m, n, k, and l. The side length of PSF vignettes is $128\lambda/D$.

with centered obscuration). This advantage may be of some practical importance during the manufacturing or development process.

In Fig. 4, typical PSF intensities formed by azimuthal cosine functions having variable indices n and k are reproduced into vignettes of $128\lambda/D$ side length each. Their general aspect is that of a dark central region surrounded by $2k$ satellite intensity peaks. Only a careful examination of the side diffraction lobes reveals that the symmetry order of the PSF pattern is actually equal to $2k$ when k is even and to k when it is an odd number. One also notes that the angular size of the nulled area is regularly increasing with the index k, and that the strength of the sidelobes also increases with the index n corresponding to higher values of $z_{0,n}$. As in the previous subsection, we also checked that the central null is preserved with variable amounts of defocus (not shown in the figure).

Finally, it must be emphasized that similar cases of phase functions $\varphi_a(\theta)$ have already been reported in the literature. They were first mentioned by Dyson in the same paper where he describes circular gratings [22], but without discussing their nulling properties. Later, Ojeda-Castañeda *et al.* [23] described discontinuous azimuthal functions generating null axial irradiances. Also, Topuzoski and Janicijevic [24] studied the properties of continuous phase functions when illuminated by Gaussian laser beams. To our knowledge, however, this is the first time that the necessary condition $\varphi_a(\theta) = z_{0,n}\cos(k\theta + l\pi/2)$ for generating axial nulls is formulated.

3. Discontinuous Azimuthal Cosine Functions

As can be seen in Fig. 3, the azimuthally cosine-modulated phase functions $\varphi_a(\theta)$ presented in the previous paragraph are all centrosymmetric. As well, the irradiance distributions they form at the image plane can be seen in Fig. 4. However, such central symmetry is not a necessary condition for achieving a central null. As a counterexample one may consider the discontinuous azimuthal cosine (DAC) phase function,

$$\varphi_a(\theta) = z_{0,n}\cos[(k + 1/2)\theta], \tag{10}$$

where $\theta \in [0.2\pi]$, $z_{0,n}$ is the nth zero of the type-J Bessel function $J_0(z)$, and k is the same index as previously. It is not difficult to show that this function also generates a central extinction, since its Strehl ratio $S_\theta(z)$ is equal to $2\pi J_0(z)$ for any k number (see Appendix A).

The properties of these DAC phase functions are illustrated in Fig. 5, showing their interferograms and resulting intensity distributions when $k = 2$ (panels A and B) and $k = 3$ (panels C and D). The interferograms first reveal an azimuthal discontinuity along the X-axis at the polar angle $\theta = 0$. From Eq. (10) this phase jump is equal to $2z_{0,n}$ waves, since $\varphi_a(\theta)$ tends toward $z_{0,n}$ when $\theta \to 0$ and $-z_{0,n}$ when $\theta \to 2\pi$. Second, the PSF in vignettes B and D have lost their centrosymmetry with respect to point O', but still exhibit a symmetry with respect to the Y'-axis. These intensity maps may also be considered as intermediate cases between those presented on the first horizontal strip of Fig. 4.

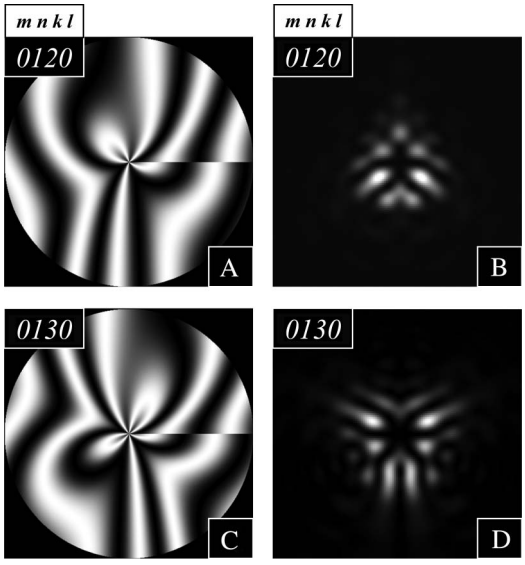

Fig. 5. Interferograms (panels A and C) and intensity distributions (B and D) produced by two discontinuous cosine functions $\varphi_a(\theta)$ defined by Eq. (10). The four digits indicate the index values m, n, k, and l. Interferograms are shown with two fringes of vertical tilt. The side length of PSF vignettes is $128\lambda/D$.

Another interesting property of DAC functions is their carried OAMs, which is discussed in the next subsection.

4. Orbital Angular Momentum

Although not the main scope of this paper, it is quite easy to estimate the OAM of the presented azimuthal phase functions. Following [25] and under the hypotheses and notations employed in this paper, the OAM generated by a uniformly illuminated pupil and normalized with respect to the total intensity gives in the pupil plane

$$\mathrm{OAM} = \mathrm{Im}\left[\int_{\rho=0}^{1}\int_{\theta=0}^{2\pi} a^*(\rho,\theta)\frac{\partial a(\rho,\theta)}{\partial\theta}\rho\mathrm{d}\rho\mathrm{d}\theta\right] \Big/\!/ \int_{\rho=0}^{1}\int_{\theta=0}^{2\pi}\rho\mathrm{d}\rho\mathrm{d}\theta, \tag{11a}$$

where Im denotes the imaginary part of a complex number, $*$ is its complex conjugate, and

$$a(\rho,\theta) = \exp[i(\varphi_r(\rho) + \varphi_a(\theta))]. \tag{11b}$$

Then Eqs. (11) readily reduce to

$$\mathrm{OAM} = \frac{1}{2\pi}\int_0^{2\pi}\frac{\partial\varphi_a(\theta)}{\partial\theta}\mathrm{d}\theta = \frac{\varphi_a(2\pi) - \varphi_a(0)}{2\pi}. \tag{12}$$

For linear azimuthal phase ramps, the previous relation promptly leads to a normalized OAM equal to mk, which is the expected result. For a cosine-modulated phase as defined in Subsection 3.A.2, it is found that OAM $= 0$, which is compliant with demonstrations using a quantum optics formalism [26]. For the DAC functions of Subsection 3.A.3, however, it yields

$$\mathrm{OAM} = \frac{z_{0,n}}{2\pi}[\cos[2\pi(k+1/2)] - 1] = -\frac{z_{0,n}}{\pi}. \tag{13}$$

This is an unusual example of an optical beam carrying a noninteger OAM and still producing full central extinction. Assuming that the term "vortex" is reserved to optical beams carrying an OAM differing from zero, this last result raises some questions about how the expressions optical vortex, central null, and optical singularity are interpreted in the present paper.

(1) There is no straightforward relation between OAM and the null it may form at the image plane center. For example, the continuous cosine-modulated phase functions $\varphi_a(\theta)$ defined in Subsection 3.A.2 do not carry any OAM, while actually generating central nulls.

(2) Conversely, the presence of an OAM is not sufficient for a beam to create a central null. For example, it can easily be verified that the Strehl ratios of linear phase ramps having noninteger topological charge are not strictly equal to zero, hence their extinction is incomplete.

Therefore, the notions of optical vortex and central null are not equivalent, none of them ensuring the existence of the other. Other examples of nonvortex beams generating central nulls are the axis-symmetric phase functions $\varphi_r(\rho)$ described in forthcoming Subsection 3.B and Section 4.

The term "singularity" itself also has several different meanings. From the experimental point of view, it is often associated with the intrinsic stability of a vortex beam affected by slight lateral misalignments in the optical system. Using this definition a singularity is basically equivalent to a vortex in the framework of first-order Fourier optics to which this study is restricted, because the PSFs are invariant and thus stable in the whole field of view of the optical system. Practically, these favorable conditions are respected if the diffracting elements are located at the exit pupil of the system, or in optically conjugated planes.

Finally, there exist other relevant definitions of optical singularities, referring either to the undetermined value of phase function s at the pupil center, to phase jumps encountered on the $[0.2\pi]$ contour, or to more rigorous mathematical concepts [27]. Discussing them exhaustively is, however, beyond the initial scope of this study.

B. Axis-Symmetric Phase Functions

As in Subsection 3.A, we first write the necessary condition for an axis-symmetric phase function $\varphi_r(\rho)$ to generate zero irradiance at the center of the image plane:

$$S_r = \int_0^1 \exp[i\varphi_r(\rho)]\rho\mathrm{d}\rho = 0. \tag{14}$$

Making use of the same basic mathematical relation (7), and setting $t = 2k\pi\rho^2 + l\pi/2$ into its integral and neglecting the Gouy phase-shift terms, trivial solutions for $\varphi_r(\rho)$ can be written as

$$S_r(z) = J_m(z)/2 = \int_0^1 \exp[i\{z\cos(2k\pi\rho^2 + l\pi/2) + 2mk\pi\rho^2\}]\rho\mathrm{d}\rho. \tag{15}$$

Hence the condition $S_r(z) = 0$ implies that

$$\varphi_r(\rho) = z_{m,n} \cos(2k\pi\rho^2 + l\pi/2) + 2mk\pi\rho^2, \quad (16)$$

where $z_{m,n}$ are again the zeros of the $J_m(z)$ functions and the indices m, n, k, and l play the same role as in Subsection 3.A, this time with respect to the phase function $\varphi_r(\rho)$.

1. Pure Defocus

The case when $n = 0$ and $m \neq 0$ leads to an axis-symmetric function $\varphi_r(\rho) = 2mk\pi\rho^2$. This is the most trivial solution for achieving a central null, corresponding to an axial defocusing of the image plane with respect to its nominal position. Here the necessary condition for obtaining a zero-irradiance at the center is that $\varphi_r(\rho)$ must be a multiple of 2π. Remembering that the phase error associated with a defocus dz also writes $\varphi_r(\rho) = \pi dz R^2\rho^2/\lambda F^2$ following the notations in Fig. 1 and that ρ is a reduced pupil coordinate, it is found that the locations of the nulls along the Z-axis are multiples of the quantity $dz = 2\lambda F^2/R^2$. This is an academic result appearing in [28], Section 8.8.

2. Radial Cosine Modulation

A last trivial solution is found when setting the index m to zero, leading to the axis-symmetric function $\varphi_r(\rho) = z_{0,n} \cos(2k\pi\rho^2 + l\pi/2)$. This is an aperiodic cosine function of variable frequency that will be designated by the acronym ACVF in the following. This type of function is illustrated in the lower right panel of Fig. 6, showing an example of an interferogram where 10 fringes of tilt at 45 deg were added for the sake of illustration (one may recognize in this picture some resemblance with polishing errors of large mirrors, sometimes affected with high spatial frequency defects near their rim). In the five other vignettes are displayed gray-level maps of the produced PSF for variable index values n, k, and l. They exhibit a few similarities with respect to those presented in Subsection 3.A.2 for azimuthal phase functions, such as enlargement of the central darkened area with index k, or strength enhancement of the external diffraction rings with index n. We also observe the effects of changing the value of index l from 0 to 1, which is equivalent to replacing the cosine function in $\varphi_r(\rho)$ with a sine function, still preserving the nulled region at the center but decreasing its width and inverting the contrast within the side rings area (bottom left panel of the figure). Finally, it must be noticed that the general definition of $S_r(z)$ in Eq. (15) implies that the ACVF function can be associated with discrete amounts of defocusing (as defined in the previous paragraph) without destroying the axial null. This was confirmed by additional numerical simulations that are not presented in this paper.

Although being rigorous mathematical solutions of Eq. (14), the ACVF solutions do not provide sharp PSF intensity distributions in the image plane of an optical system. For that purpose we should rather envisage true periodic functions, i.e., circular gratings with equally spaced lines that are the scope of the next section.

4. APPLICATION TO CIRCULAR GRATINGS

Since the original work of Dyson [22], circular gratings have been the subject of numerous studies and papers. In their most popular versions, they appear as a set of equally spaced, concentric circular slits [29]. Unequally spaced line gratings have also been designed, such as circular Dammann gratings [30]. These types of gratings intrinsically suffer from transmission losses, and their efficiency is even more degraded by important energy leaks at the central lobe of their PSF. Hence the purpose of this section is twofold:

– to define circular phase gratings (CPGs) built from continuous phase functions $\varphi_r(\rho)$ without line or groove obscuring factors,

– to impose a null SR constraint (or zero-irradiance at the PSF center) in order to maximize the concentrated flux in the side diffraction rings.

Moreover, here consideration is given only to cosine phase functions of amplitude z fulfilling the condition

$$S_r(z) = \int_0^1 \exp[iz \cos(2k\pi\rho)]\rho d\rho = 0. \quad (17)$$

At first glance the integral in Eq. (17) may look intractable, and the relation (7) cannot help in solving it. However, it can

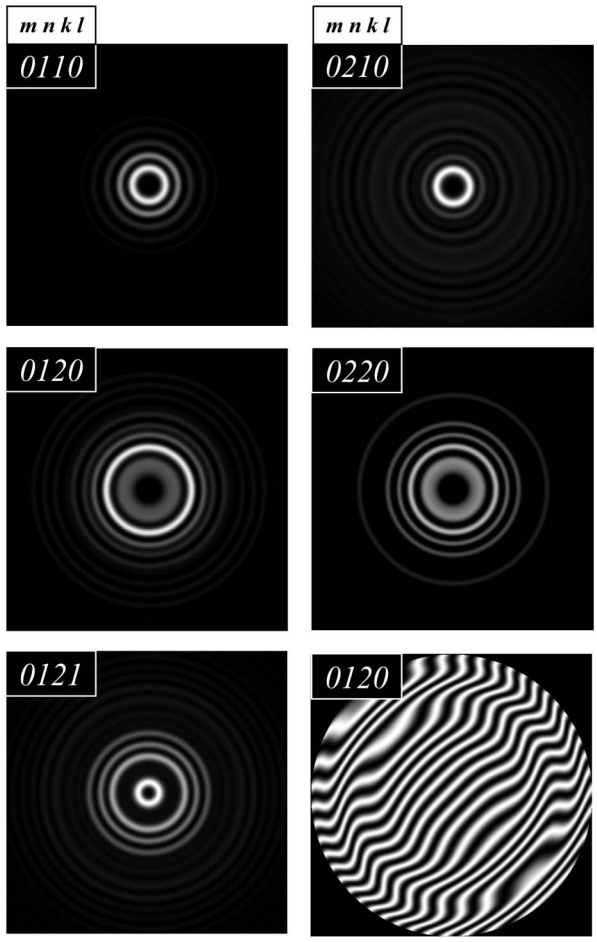

Fig. 6. Intensity distributions produced by an axis-symmetric ACVF phase function. The four digits indicate the index values m, n, k, and l. The side length of PSF vignettes is $128\lambda/D$. The lower right panel depicts one example of interferogram with 10 fringes of tilt at 45 deg.

be demonstrated that $S_r(z) = J_0(z)/2$, where $J_0(z)$ is again the type-J Bessel function of zero order (see Appendix B). Hence the necessary condition for achieving the null Strehl ratio is

$$\varphi_r(\rho) = z_{0,n} \cos(2k\pi\rho). \tag{18}$$

One can see that from the four integers m, n, k, and l defined in Section 3, only n and k remain meaningful, being respectively proportional to the amplitude and frequency of the cosine-modulated phase function. In the upper part of Fig. 7 are shown four gray-scale maps of the generated PSF in the focal plane of the optics, for indices $n = 1$ and k ranging from 1 to 4. As expected they reveal large and centered nulled areas of regularly increasing size, limited by a bright double-side diffraction ring concentrating most of the incoming power. Slices of the irradiance patterns along the X'-axis and normalized for constant PSF energy are given in the lower part of the figure. The curves confirm the existence of a dual structure diffraction pattern where the weaker ring is always located inside the brightest. This specific behavior of CPGs was already reported in [31] where under some approximations it was demonstrated that only a phase-shifted cosine function can generate a single diffraction ring. However, our numerical simulations (not reproduced here) proved that the Strehl ratio is not totally canceled in that case, unless making use of property P2 in Section 2 and adding to $\varphi_r(\rho)$ one of the azimuthal phase functions $\varphi_a(\theta)$ defined in Subsection 3.B. Also, it has been verified that increasing the indices n (i.e., $n \geq 2$) has the same consequences as in Section 3, reinforcing the optical power in the external diffraction rings and consequently reducing the CPG efficiency. This means that the optimal choice for the phase amplitude is limited to $z_{0,1}$ in practice.

By definition a diffraction grating operates over a finite spectral band, and the PSF formed in the image plane varies as function of wavelength. It implies that the central extinction generated by a nulling CPG shall be maintained over its full spectral range, or at least inferior to a certain limit. Numerical simulations were then undertaken for a CPG optimized at a reference wavelength $\lambda_0 = 0.5$ μm and indices $n = 1$ and $k = 4$. Their results are illustrated in Fig. 8, showing the intensity distributions produced at λ_0, $\lambda = 0.52$ μm and $\lambda = 0.54$ μm. The three gray-level maps on the top clearly illustrate the progressive emergence of a parasitic peak at the PSF center. In the lower panel of the figure is also plotted the central intensity peak value as a function of the wavelength λ. Assuming that for high k numbers the power enclosed in the central lobe of the PSF remains negligible with respect to the energy radiated in the first ring, one may empirically define the useful spectral range of the CPG as the wavelength domain where the central PSF peak remains inferior to the brightest diffracted ring (this criterion is indicated by dashed lines in the figure). In this particular example it would be estimated as $\delta\lambda = 0.462$–0.542 μm, corresponding to $\delta\lambda/\lambda = 16.5\%$.

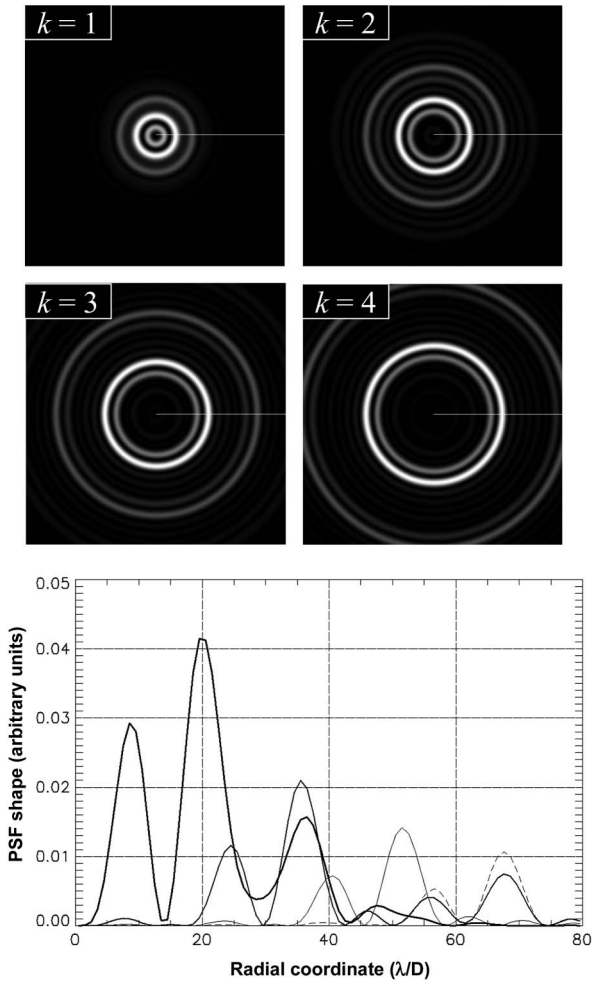

Fig. 7. Intensity distributions produced by equally spaced circular phase gratings for $n = 1$ and increasing values of the k index. (Bottom) X'-slices of the PSF along the thin white lines. The side length of PSF vignettes is $128\lambda/D$.

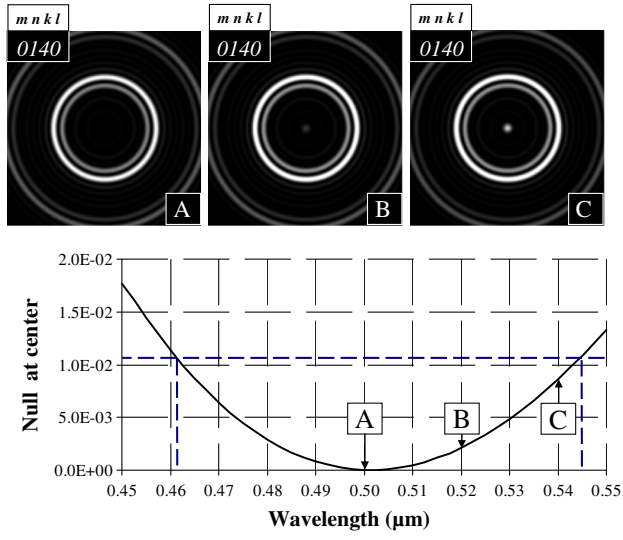

Fig. 8. Influence of wavelength on the central null in the case of an equally spaced circular phase grating with $n = 1$ and $k = 4$. (Top) Intensity distributions produced at the reference wavelength $\lambda_0 = 0.5$ μm (A), $\lambda = 0.52$ μm (B), and $\lambda = 0.54$ μm (C). (Bottom) Curve of the peak intensity at PSF center versus λ.

As for all phase functions presented in this paper, we finally studied the influence of defocusing the axial null, finding its degradation to be much slower than on the diffraction rings with identical amounts of aberration. Thus it can be concluded that a typical "diffraction-limited" requirement (e.g., WFE inferior to $\lambda/4$ peak-to-valley) should be sufficient for preserving good on-axis light rejection, at least when extreme nulling rates are not desired.

5. COMPLEX APERTURE SHAPES

In Sections 3 and 4 this study was restricted to phase functions $\varphi_a(\theta)$ and $\varphi_r(\rho)$ generating null Strehl ratios from a nonobstructed circular pupil of radius R. Discussed below are the effects of more complex, truncated aperture shapes that can be geometrically described by the amplitude apodizing functions $t_r(\rho)$ and $t_a(\theta)$ appearing in Eq. (4). The effects of pupil truncation or masking can be summarized into five additional properties of the nulling phase functions $\varphi_a(\theta)$ and $\varphi_r(\rho)$:

- P4. Central nulls generated by azimuthal phase functions $\varphi_a(\theta)$ will not be affected by any axis-symmetric obscuration $t_r(\rho)$ centered in the pupil plane.
- P5. Similarly, central nulls generated by axis-symmetric phase functions $\varphi_r(\rho)$ will not be affected by any azimuthal truncation $t_a(\theta)$ in the pupil plane.
- P6. Axis-symmetric phase functions $\varphi_r(\rho)$ generating central nulls from a full circular pupil can be rescaled so as to preserve the central null in the presence of axis-symmetric obscuration $t_r(\rho)$.
- P7. Similarly, azimuthal phase functions $\varphi_a(\theta)$ generating central nulls from a full circular pupil can be rescaled so as to preserve the central null in the presence of azimuthal truncation $t_a(\theta)$.
- P8. Different types of phase functions $\varphi_r(\rho)$ or $\varphi_a(\theta)$ generating a central null from different subapertures with azimuthal truncation $t_a(\theta)$ or axis-symmetric obscuration $t_r(\rho)$ can be juxtaposed within a single circular aperture, and still produce together a central null.

Some of the previous properties will be illustrated with the help of a few examples provided in the three following subsections: Subsection 5.A deals with the simplest case of unaffected phase functions (P4 and P5), Subsection 5.B explains how to rescale their pupil coordinates when needed (P6), and Subsection 5.C shows how they can be combined spatially (P8). It must be noted that the properties P4, P7, and P8 have already been reported for optical vortices of integer order m [12,32].

A. Case of Unmodified Phase Functions

From P4 and P5, one or several axis-symmetric pupil masks should not alter the extinction produced by a nulling azimuthal phase function, and reciprocally. Using the polar coordinates θ and ρ in Fig. 1, such masks generally appear as a sectioned ring shown in the lower part of the figure, where θ and ρ are bounded by four known geometrical parameters.

Azimuthal truncation:	$t_a(\theta). = 1$ if $\theta_1 \le \theta \le \theta_2$ and $t_a(\theta). = 0$ elsewhere,
Axis-symmetric mask:	$t_r(\rho). = 1$ if $\rho_1 \le \rho \le \rho_2$ and $t_r(\rho). = 0$ elsewhere (for a central obscuration, ρ_1 is the obscuration rate and $\rho_2 = 1$).

In Fig. 9, panels A and B illustrate the case of a cosine azimuthal phase function $\varphi_a(\theta)$ with indices m, n, k, and l equal to 0, 3, 4, and 0, respectively. The phase function is obscured by a circular ring from $\rho = 0.3$ to $\rho = 0.7$, that is actually the addition of two axis-symmetric masks with $(\rho_1, \rho_2) = (0, 0.3)$ and $(\rho_1, \rho_2) = (0.7, 1)$. In A is shown a picture of the masked interferogram with 10 fringes of tilt at 45 deg. The gray-level map of the resulting PSF is provided in the vignette B. It has to be compared with the reference intensity distribution formed by the unmasked pupil appearing in the lower left corner of Fig. 4. One can see that the central null is left unaltered, in spite of visible enhancement of the side diffraction lobes due to the presence of the mask.

Also in Fig. 9, Panels C and D provide an example of an azimuthally truncated pupil in the form of a four-branch Siemens star (panel C), standing for a quadripod supporting the secondary mirror of a telescope. This case may be of special interest for vortex coronagraph applications [15–17], where the usual support legs of constant thickness are harmful to the central extinction. Here this mask has been applied to a CPG with indices $n = 1$ and $k = 4$, thereby generating the intensity distribution reproduced in panel D of Fig. 9 (the reference PSF with no pupil obscuration is shown in Fig. 7). It can be verified that the dark central area is unchanged, though the effect of the four star branches is clearly visible on the bright diffraction rings. It must also be noticed that for the sake of realism the pupil mask also includes a minimal central obscuration by a factor $\rho_1 = 0.1$. Therefore, the CPG function $\varphi_r(\rho)$ also had to be rescaled along the aperture radius, following the rules explained next in Subsection 5.B.

B. Phase Scaling in Truncated Apertures

When an axis-symmetric phase function $\varphi_r(\rho)$ or an azimuthal phase function $\varphi_a(\theta)$ is associated with the same type of pupil mask function [respectively $t_r(\rho)$ and $t_a(\theta)$], the expressions of the radial and azimuthal Strehl ratios S_r and S_a in Eqs. (5b) and (5c) become

$$S_r = \int_{\rho_1}^{\rho_2} \exp[i\varphi_r(\rho)]\rho \mathrm{d}\rho, \tag{19a}$$

$$S_a = \int_{\theta_1}^{\theta_2} \exp[i\varphi_a(\theta)]\mathrm{d}\theta. \tag{19b}$$

Then the necessary conditions for attaining a central extinction $S_r = 0$ and $S_a = 0$ can only be fulfilled by changing the

Table 1. Summary of Rescaling Coordinates Usable for Different Nulling Phase Functions

Name and Section	Phase Function/ Rescaling Coordinate
Linear and cosine azimuthal functions, § 3.A	$\varphi_a(\theta) = z_{m,n}\cos(k\theta' + l\pi/2) + mk\theta'$ $\theta' = (\theta - \theta_1)/(\theta_2 - \theta_1)$
Aperiodic cosine function (ACVF), § 3.B	$\varphi_r(\rho) = z_{m,n}\cos(2k\pi\rho'^2 + l\pi/2)$ $+2mk\pi\rho'^2$ $\rho'^2 = (\rho^2 - \rho_1^2)/(\rho_2^2 - \rho_1^2)$
Circular phase grating (CPG), § 4	$\varphi_r(\rho) = z_{0,n}\cos(2k\pi\rho')$ $\rho' = (\rho - \rho_1)/(\rho_2 - \rho_1)$

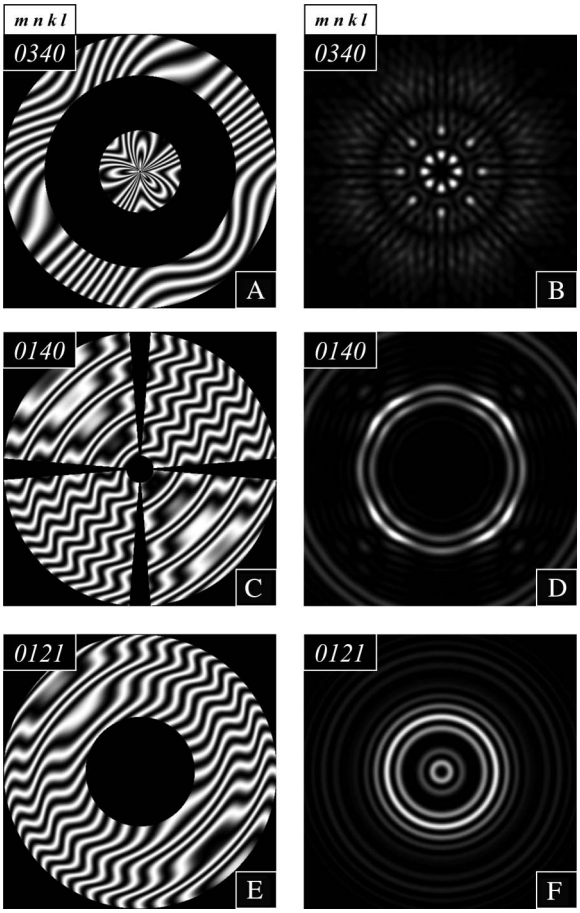

Fig. 9. Preservation of the central null generated by phase functions $\varphi_a(\theta)$ or $\varphi_r(\rho)$ with complex aperture shapes. A and B, case of a cosine azimuthal phase function $\varphi_a(\theta)$ of indices 0, 3, 4, and 0, obscured by a circular ring from $\rho = 0.3$ to $\rho = 0.7$, illustrated by an interferogram (A) and the resulting PSF (B). C and D, Case of a CPG function $\varphi_r(\rho)$ with indices $n = 1$ and $k = 4$, with an axis-symmetric quadripod and a central obscuration $\rho_1 = 0.1$, illustrated by the interferogram (C) and PSF (D). E and F, Case of an ACVF phase function $\varphi_r(\rho)$ of indices 0, 1, 2 and 1 fitted to a central obscuration $\rho_1 = 0.4$, illustrated by the interferogram (E) and PSF (F). All interferograms are shown with 10 fringes of tilt at 45 deg and the side length of PSF vignettes is $128\lambda/D$. The reference PSFs are respectively shown in Figs. 4, 7, and 6.

integration variables ρ and θ, leading to the definition of new coordinates ρ' and θ' in order to rescale the integration domains. In Table 1 is given, for each type of phase function $\varphi_r(\rho)$ and $\varphi_a(\theta)$ appearing in this paper, the mathematical relationships usable for defining the rescaling coordinates and thus ensuring PSF axial extinction.

Finally, presented in panels E and F of Fig. 9 is the case of an ACVF phase function $\varphi_r(\rho)$ of indices 0, 1, 2, and 1 fitted to a central obscuration $\rho_1 = 0.4$, illustrated by its interferogram (E) and the resulting PSF (F). When confronted to its reference intensity distribution in the lower left corner of Fig. 6, one can see that the central null is still unaffected, but accompanied by an apparent energy leak toward the outer PSF rings caused by phase function rescaling.

C. Spatial Combination of Phase Functions

From the above properties P4 to P7 and elementary addition of the integral domains, it is straightforward to demonstrate that all types of phase function $\varphi_r(\rho)$ and $\varphi_a(\theta)$ defined and eventually scaled so as to respect the conditions $S_r = 0$ or $S_a = 0$ over nonintersecting subapertures $t_r(\rho)$ and $t_a(\theta)$, can be spatially combined into a single circular pupil and together produce an axial null. This probably opens the door to a vertiginous infinity of such "mixed" phase functions having the ability to generate central extinctions of various sizes. It is the reason why only one example is provided here, based on arbitrary parameters. This is the case illustrated in Fig. 10, where the phase function is composed of a linear azimuthal phase ramp of topological charge 4 delimited by $\rho_1 = 0.1$

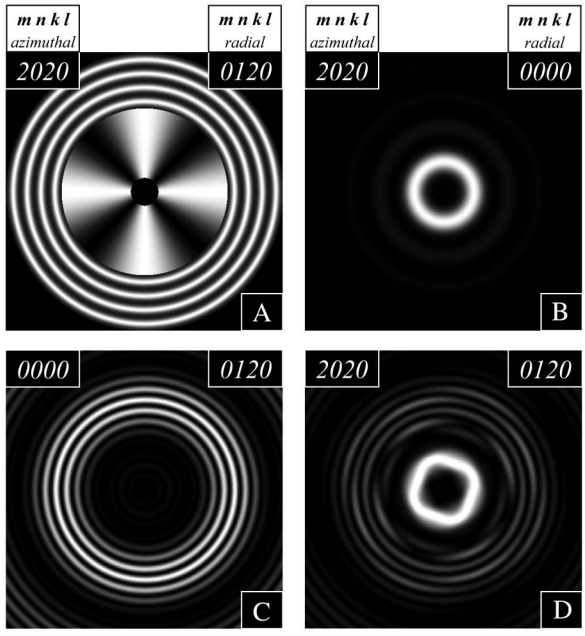

Fig. 10. Juxtaposition of two phase functions in the exit pupil plane; from a linear azimuthal phase ramp of topological charge 4 delimited by $\rho_1 = 0.1$ and $\rho_2 = 0.6$, and an ACVF phase function of indices $j = 1$ and $k = 2$ delimited by $\rho_1 = 0.6$ and $\rho_2 = 1$. A, Interferogram of the composed WFE; B, PSF generated by the linear azimuthal phase ramp alone; C, PSF generated by the ACVF alone; D, PSF generated by the mixed phase function. The side length of PSF vignettes is $128\lambda/D$.

and $\rho_2 = 0.6$, and of a square-cosine axis-symmetric phase function with indices $j = 1$ and $k = 2$, limited by $\rho_1 = 0.6$ and $\rho_2 = 1$. The figure shows the resulting interferogram (panel A), individual PSF generated by each of the individual phase functions (panels B and C), and the PSF resulting from their juxtaposition (panel D). As expected the central null is preserved, but one also notes a loss of axis-symmetry due to the presence of the linear azimuthal phase ramp.

Many other interesting examples of composed phase functions could have been added in this section. It is likely, however, that identifying the most promising solutions can only be achieved using automated searching software, specially developed for that purpose.

6. CONCLUSION

In this paper a set of radial and azimuthal phase functions $\varphi_r(\rho)$ and $\varphi_a(\theta)$ were reviewed that have a null Strehl ratio, which is equivalent to generating a null at the center of the image plane of an optical system. This study was conducted in the framework of Fraunhofer far-field scalar diffraction, and oriented toward practical cases where the on-axis extinction is produced by means of a deformable mirror or phase plates. The identified solutions revealed unexpected links with the zeros of type-J Bessel functions of integer order. They include linear azimuthal phase ramps giving birth to an optical vortex, azimuthally modulated phase functions and CPGs. It was found in particular that the CPG radiometric efficiency could be significantly improved by the null SR condition. Simple design rules for rescaling and combining these different phase functions were also defined or revisited.

In this study only analytical and continuous phase functions fulfilling the central null condition were considered. It can be reasonably conjectured that other analytical solutions exist, including a number of discontinuous or stepped functions built from the previous solutions. More generally, it is likely that the same approach could be followed in a fully numerical manner, looking for either discrete or continuous phase shapes. We finally note that, although not addressed in this paper, the search for null Strehl ratios can be extended to the pupil apodizing functions $t_r(\rho)$ and $t_a(\theta)$, as defined in Section 2. This may obviously lead to already known amplitude profiles, such as Laguerre–Gauss polynomials [12], but it may also lead to identifying new classes of complex amplitude functions enabling the generation of various sorts of optical nulls and singularities. In this respect, the analytical solutions described in this paper could serve as starting points for an automated searching software tool.

APPENDIX A: COMPUTING FUNCTION $S_\theta(Z)$ FOR DISCONTINUOUS COSINE PHASE DISTRIBUTIONS (DAC)

In this appendix is demonstrated the identity

$$S_\theta(z) = \int_0^{2\pi} \exp[iz\cos[(k+1/2)\theta]]\mathrm{d}\theta = 2\pi J_0(z), \quad \textbf{(A1)}$$

for any integer k. Setting the new variable $t = (k+1/2)\theta$ into the integral, $S_\theta(z)$ becomes

$$S_\theta(z) = \frac{1}{k+1/2}\int_0^{2k\pi+\pi} \exp[iz\cos t]\mathrm{d}t. \quad \textbf{(A2)}$$

Applying Eq. (7) with $m = l = 0$ one finds

$$S_\theta(z) = \frac{2k\pi J_0(z)}{k+1/2} + \frac{1}{k+1/2}\int_0^{\pi} \exp[iz\cos t]\mathrm{d}t. \quad \textbf{(A3)}$$

Simple integral manipulation and again employing Eq. (7) also leads to

$$\int_0^{\pi} \exp[iz\cos t]\mathrm{d}t = \int_{-\pi}^{0} \exp[iz\cos t]\mathrm{d}t = \frac{1}{2}\int_{-\pi}^{+\pi} \exp[iz\cos t]\mathrm{d}t = \pi J_0(z). \quad \textbf{(A4)}$$

Inserting Eq. (A4) into Eq. (A3), it directly follows that $S_\theta(z) = 2\pi J_0(z)$, hence demonstrating Eq. (A1).

APPENDIX B: COMPUTING FUNCTION $S_R(Z)$ FOR CIRCULAR PHASE GRATINGS (CPG)

In this appendix is demonstrated the equality

$$S_r(z) = \int_0^1 \exp[iz\cos(2k\pi\rho)]\rho\mathrm{d}\rho = J_0(z)/2, \quad \textbf{(B1)}$$

for any integer $k \neq 0$. First setting a new variable $t = 2\pi\rho$ into the integral, $S_r(z)$ can be rewritten as

$$S_r(z) = \int_0^{2\pi} \exp[iz\cos kt]t\mathrm{d}t/4\pi^2, \quad \textbf{(B2)}$$

or, separating the real and imaginary parts,

$$S_r(z) = \left(\int_0^{2\pi} \cos(z\cos kt)t\mathrm{d}t + i\int_0^{2\pi} \sin(z\cos kt)t\mathrm{d}t\right)/4\pi^2, \quad \textbf{(B3)}$$

where $i = \sqrt{-1}$. Developing the cosine and sine functions according to Jacobi's identities [20]:

$$\cos(z\cos t) = J_0(z) + 2\sum_{n=1}^{+\infty}(-1)^n J_{2n}(z)\cos(2nt), \quad \textbf{(B4)}$$

$$\sin(z\cos t) = 2\sum_{n=0}^{+\infty}(-1)^n J_{2n+1}(z)\cos((2n+1)t), \quad \textbf{(B5)}$$

the real and imaginary parts of $S_r(z)$ can be written as

$$\mathrm{Real}[S_r(z)] = J_0(z)/2 + \sum_{n=1}^{+\infty}(-1)^n J_{2n}(z)\int_0^{2\pi}\cos(2nkt)t\mathrm{d}t/2\pi^2, \quad \textbf{(B6)}$$

$$\mathrm{Im}[S_r(z)] = \sum_{n=1}^{+\infty}(-1)^n J_{2n+1}(z)\int_0^{2\pi}\cos((2n+1)kt)t\mathrm{d}t/2\pi^2. \quad \textbf{(B7)}$$

Simple integration by parts allows demonstrating that $\int_0^{2\pi}\cos(nt)t\mathrm{d}t = 0$ for any integer $n \neq 0$, finally leading to $S_r(z) = J_0(z)/2$ and demonstrating Eq. (B1).

The author would like to thank the anonymous reviewers for their inspiring comments, and his colleague P. Rabou for careful reading of the manuscript and improvement of English wording.

REFERENCES

1. M. E. J. Friese, J. Enger, H. Rubinsztein-Dunlop, and N. R. Heckenberg, "Optical angular-momentum transfer to trapped absorbing particles," Phys. Rev. A **54**, 1593–1596 (1996).
2. J. Leach, M. J. Padgett, S. M. Barnett, S. Franke-Arnold, and J. Courtial, "Measuring the orbital angular momentum of a single photon," Phys. Rev. Lett. **88**, 257901 (2002).
3. Z. Tong and O. Korotkova, "Beyond the classical Rayleigh limit with twisted light," Opt. Lett. **37**, 2595–2597 (2012).
4. R. K. Tyson, M. Scipioni, and J. Viegas, "Generation of an optical vortex with a segmented deformable mirror," Appl. Opt. **47**, 6300–6306 (2008).
5. G. Campbell, B. Hage, B. Buchler, and P. K. Lam, "Generation of high-order optical vortices using directly machined spiral phase mirrors," Appl. Opt. **51**, 873–876 (2012).
6. G. A. Turnbull, D. A. Robertson, G. M. Smith, L. Allen, and M. J. Padgett, "The generation of free-space Laguerre-Gaussian modes at millimetre-wave frequencies by use of a spiral phaseplate," Opt. Commun. **127**, 183–188 (1996).
7. N. R. Heckenberg, R. McDuff, C. P. Smith, and A. G. White, "Generation of optical phase singularities by computer-generated holograms," Opt. Lett. **17**, 221–223 (1992).
8. M. Reicherter, T. Haist, E. U. Wagemann, and H. J. Tiziani, "Optical particle trapping with computer-generated holograms written on a liquid-crystal display," Opt. Lett. **24**, 608–610 (1999).
9. M. W. Beijersbergen, L. Allen, H. E. L. O. van der Veen, and J. P. Woerdman, "Astigmatic laser mode converters and transfer of orbital angular momentum," Opt. Commun. **96**, 123–132 (1993).
10. P. Vaity, A. Aadhi, and R. P. Singh, "Formation of optical vortices through superposition of two Gaussian beams," Appl. Opt. **52**, 6652–6656 (2013).
11. J. García-García, C. Rickenstorff-Parrao, R. Ramos-García, V. Arrizón, and A. S. Ostrovsky, "Simple technique for generating the perfect optical vortex," Opt. Lett. **39**, 5305–5308 (2014).
12. A. M. Yao and M. J. Padgett, "Orbital angular momentum: origins, behavior and applications," Adv. Opt. Photonics **3**, 161–204 (2011).
13. A. Ferrari, R. Soummer, and C. Aime, "An introduction to stellar coronagraphy," C. R. Phys. **8**, 277–287 (2007).
14. O. Guyon, E. A. Pluzhnik, M. J. Kuchner, B. Collins, and S. T. Ridgway, "Theoretical limits on extrasolar terrestrial planet detection with coronagraphs," Astrophys. J. **167**, 81–99 (2006).
15. D. Mawet, P. Riaud, O. Absil, and J. Surdej, "Annular groove phase mask coronagraph," Astrophys. J. **633**, 1191–1200 (2005).
16. G. A. Swartzlander, Jr., "The optical vortex coronagraph," J. Opt. A: Pure Appl. Opt. **11**, 094022 (2009).
17. D. Mawet, E. Serabyn, K. Liewer, R. Burruss, J. Hickey, and D. Shemo, "The vector vortex coronagraph: laboratory results and first light at Palomar Observatory," Astrophys. J. **709**, 53–57 (2010).
18. V. N. Mahajan, "Strehl ratio for primary aberrations: some analytical results for circular and annular pupils," J. Opt. Soc. Am. **72**, 1258–1266 (1982).
19. T. S. Ross, "Limitations and applicability of the Maréchal approximation," Appl. Opt. **48**, 1812–1818 (2009).
20. M. Abramowitz and I. A. Stegun, *Handbook of Mathematical Functions* (Dover Publications, 1972).
21. V. V. Kotlyar, A. A. Almazov, S. N. Khonina, V. A. Soifer, H. Elfstrom, and J. Turunen, "Generation of phase singularity through diffracting a plane or Gaussian beam by a spiral phase plate," J. Opt. Soc. Am. A **22**, 849–861 (2005).
22. J. Dyson, "Circular and spiral diffraction gratings," Proc. R. Soc. London A **248**, 93–106 (1958).
23. J. Ojeda-Castañeda, P. Andrés, and M. Martínez-Corral, "Zero axial irradiance by annular screens with angular variation," Appl. Opt. **31**, 4600–4602 (1992).
24. S. Topuzoski and L. Janicijevic, "Diffraction characteristics of optical elements designed as phase layers with cosine-profiled periodicity in the azimuthal direction," J. Opt. Soc. Am. A **28**, 2465–2472 (2011).
25. S. N. Khonina, V. V. Kotlyar, V. A. Soifer, P. Paakkonen, J. Simonen, and J. Turunen, "An analysis of the angular momentum of a light field in terms of angular harmonics," J. Mod. Opt. **48**, 1543–1557 (2001).
26. V. V. Kotlyar, S. N. Khonina, R. V. Skidanov, and V. A. Soifer, "Rotation of laser beams with zero of the orbital angular momentum," Opt. Commun. **274**, 8–14 (2007).
27. M. R. Dennis, K. O'Holleran, and M. J. Padgett, "Singular optics: optical vortices and polarization singularities," in *Progress in Optics* (Elsevier, 2009), Vol. **53**, pp. 293–363.
28. M. Born and E. Wolf, *Principles of Optics* (Cambridge University, 1999).
29. D. Tichenor and R. N. Bracewell, "Fraunhofer diffraction of concentric annular slits*," J. Opt. Soc. Am. **63**, 1620–1622 (1973).
30. C. Zhou, J. Jia, and L. Liu, "Circular Dammann grating," Opt. Lett. **28**, 2174–2176 (2003).
31. A. Fedotowsky and K. Lehovec, "Far field diffraction patterns of circular gratings," Appl. Opt. **13**, 2638–2642 (1974).
32. R. Rop, I. A. Litvin, and A. Forbes, "Generation and propagation dynamics of obstructed and unobstructed rotating orbital angular momentum-carrying Helicon beams," J. Opt. **14**, 035702 (2012).